Measles Virus Entry Through the Signaling Lymphocyte Activation Molecule Governs Efficacy of Mantle Cell Lymphoma Radiovirotherapy

Tanner S Miest[1,2], Marie Frenzke[1] and Roberto Cattaneo[1,2]

[1]Department of Molecular Medicine, Mayo Clinic, Rochester, Minnesota, USA; [2]Virology and Gene Therapy Track, Mayo Graduate School, Rochester, Minnesota, USA

We developed here a vaccine-identical measles virus (MV) as an oncolytic agent against mantle cell lymphoma (MCL), an aggressive B-cell non-Hodgkin's lymphoma that is difficult to cure but radiosensitive. We armed the virus with the sodium-iodide symporter, which concentrates iodide within infected cells enabling noninvasive imaging and combination radiovirotherapy. Through high-resolution *in vivo* and *ex vivo* imaging, we visualized the spread of infections in primary and metastatic tumors for over 2 weeks after therapy, documenting homogeneous virus seeding and spread restricted to perfused tissue. Infection of metastases was more rapid and intense than primary tumors, achieving isotope uptake within about threefold the efficiency of the thyroid. Virotherapy combined with systemic ^{131}I resulted in more rapid disease regression than either therapy alone. In addition to ubiquitous CD46, vaccine MV retains cell entry through its immune cell-specific receptor signaling lymphocytic activation molecule (SLAM). We asked whether both receptors could sustain effective oncolysis of MCL. Strikingly, only SLAM-dependent entry sustained efficient viral spread, tumor regression, and prolonged survival. These observations shift the focus of future clinical trials to SLAM-expressing hematologic malignancies and suggest that oncolytic vectors may depend on tissue-specific receptors for both cell entry and activation of responses assisting their replication.

INTRODUCTION

Oncolytic virotherapy is an experimental therapeutic modality that harnesses the destructive power of viruses to selectively infect and kill target tumor cells.[1] Viruses can be genetically modified for greater tumor specificity and efficacy through combinations of different targeting and arming strategies.[2] As a treatment modality, oncolytic virotherapy is uniquely capable of amplification and spread within distant disease sites, and the cytopathic effect of viruses represents a new therapeutic principle and treatment option for disease states refractory to traditional chemo- and radiotherapies.

A key challenge for the oncolytic virotherapy field is documenting and understanding the mechanisms underlying therapeutic efficacy, namely vector amplification and spread within disease tissue. Toward addressing this challenge, vectors can be engineered to encode transgenes that track viral replication. For example, the sodium-iodide symporter (NIS) normally functions to concentrate iodide into follicular cells of the human thyroid during production of thyroid hormone,[3] but when expressed from the genome of viral vectors NIS can empower noninvasive imaging of virus replication.[4] In addition, NIS expression in combination with radioiodine can induce synergistic tumor cell killing by concentrating high-energy isotope within infected tumor tissue.[5]

Mantle cell lymphoma (MCL) is an aggressive subtype of B-cell non-Hodgkin Lymphoma (NHL) with one of the worst prognoses of any NHL.[6,7] MCL is characterized clinically by advanced stage disease at diagnosis with extranodal manifestation in the majority of patients, and a pattern of continuous relapse after therapy.[6,7] Current first-line therapies for MCL include chemotherapy regimens containing anthracyclines and rituximab, with myeloablative chemotherapy and autologous stem cell transplantation indicated for some patients.[6,7] Despite positive initial responses, relapse is inevitable in most patients and concurrent with therapy resistance and a more aggressive disease phenotype.[6,7] MCL is radiosensitive,[8] but the systemic nature of the disease limits the use of traditional radiotherapies. Radio-conjugated antibodies have shown promise in clinical trials,[9] motivating the development of additional strategies for applying systemic radiotherapy to the treatment of relapsed MCL.

Measles virus (MV) may be well suited for treatment of MCL because of its natural tropism for lymphocytes.[10] MV wild-type strains infect these cells through their primary receptor signaling lymphocytic adhesion molecule (SLAM).[11,12] Notably, certain SLAM-positive hematological malignancies have been observed to regress following natural contagion of MV.[13,14] SLAM is the primary receptor for all MV strains, including attenuated vaccine strains that have also adapted to use the ubiquitously expressed regulator of complement activation CD46 during attenuation.[15,16] Vaccine-lineage MV is currently being tested clinically

Correspondence: Roberto Cattaneo, Department of Molecular Medicine, Mayo Clinic, Guggenheim 18, 200 First St. SW, Rochester, Minnesota 55905, USA. E-mail: cattaneo.roberto@mayo.edu

as an oncolytic vector for ovarian cancer[17] (NCT00408590), multiple myeloma (NCT00450814), glioblastoma multiforme (NCT00390299), and mesothelioma (NCT01503177). Although these clinical trials assume that CD46 overexpression may favor vector replication in cancer tissue,[18,19] no correlation between CD46 expression levels and prolongation of life expectancy has been reported.[17] Moreover, recent studies in monkeys[20,21] indicate that CD46-dependent entry has little if any relevance for vaccine-strain MV amplification and spread in lymphocytes of permissive hosts. In the case of hematological malignancies that coexpress SLAM and CD46, little is known about the respective contributions of each receptor to the efficacy of MV oncolysis.

We have previously shown primary MCL samples and MCL xenografts to be sensitive to MV infection,[22,23] which combined with its radiosensitivity makes MCL an excellent target for therapy with NIS-expressing oncolytic MV. In this study, we generated a MV vector expressing NIS that is less attenuated than the vector currently used in clinical trials: this new strain retains its ability to interfere with STAT signaling[24] and cytosolic RNA helicase-mediated innate immunity.[25] On the basis of single photon emission computed tomography (SPECT), we document here three-dimensional spread of viral infections in primary tumors and metastases for >2 weeks following systemic therapy. We show that our oncolytic MV vector expressing NIS (i) can induce curative regression of MCL xenografts after systemic therapy, (ii) depends on SLAM but not CD46 entry for efficacy, and (iii) induces synergistic tumor killing in combination with systemic [131]I.

RESULTS

MV[vac2]NIS replicates efficiently and expresses functional NIS in MCL Granta-519 cells

We previously generated MV[vac2], a recombinant virus, whose genomic sequence is identical to that of the licensed Moraten vaccine strain of MV.[24,26] MV[vac2] differs from the composite infectious cDNA used in the first MV reverse genetics system (MV-Ed-Tag),[27] and later modified to obtain the vectors currently used in clinical trials (MV-CEA and MV-NIS);[17] in that, it codes for standard P and V proteins capable of antagonizing innate immunity. The shared amino-terminus of the P and V proteins codes for tyrosine 110, restoring STAT1 interference function,[24,28] whereas the carboxy-terminus of the V protein codes for cysteine 272, restoring mda-5 interference function (**Figure 1a**).[25,28] Moreover, MV[vac2] is less fusogenic than MV-Ed-Tag, likely the result of four amino acid differences in the F-protein.

We generated the recombinant MV[vac2]NIS by cloning the human NIS cDNA in an additional transcription unit positioned downstream of the *MV-H* gene (**Figure 1a**). We first examined the ability of MV[vac2]NIS to replicate and express functional NIS in the MCL cell line Granta-519. MV[vac2]NIS-induced minimal cell–cell fusion of these cells during infection, instead causing clumping of individual cells, whereas MV-NIS–induced formation of large syncytia (**Figure 1b**, compare second and third panels). Despite this expected difference in cytopathic effect, cytotoxicity of the two viruses was equivalent, reducing cell viability by nearly 60% on day 6 after infection (**Supplementary Figure S1**). MV[vac2]NIS and MV-NIS displayed similar growth kinetics in Granta-519 cells, with titers peaking at 10^5 TCID$_{50}$/

ml in the cell-associated fraction at 48 hours after infection (**Figure 1c**).

We then compared NIS expression and function during infection with these two viruses. Infected Vero and Granta-519 cells were incubated with ^{125}I and then washed and lysed to quantify intracellular uptake of isotope. MV[vac2]NIS-infected Vero and Granta-519 cells efficiently concentrated ^{125}I, achieving greater and earlier peak isotope uptake than MV-NIS-infected cells (**Figure 1d**). Immunoblot analysis indicated similar NIS expression kinetics for the two viruses, but only the minimally fusogenic MV[vac2]NIS maintained NIS expression and function at later time points after infection (**Figure 1d**, **Supplementary Figure S2**). These *in vitro* data indicate that the decreased fusion of MV[vac2]NIS correlates with more efficient incorporation and/or retention of iodine within infected cells.

The Moraten vaccine strain backbone of MV[vac2]NIS codes for fully functional P and V proteins that should enable more efficient replication of oncolytic MV in tumors with intact interferon (IFN) pathways.[29] In Vero cells, which are competent to respond to but not produce IFN, MV[vac2]NIS replication was largely resistant to coadministered human leukocyte IFN up to concentrations of 10,000 units/ml, whereas MV-NIS replication was inhibited in a dose-dependent manner (**Figure 1e**, left panel), consistent with abrogation of the JAK/STAT signaling pathway by the function P and V proteins of MV[vac2]NIS but not MV-NIS. In Granta-519 cells, we observed that both MV-NIS and MV[vac2]NIS were largely resistant to the inhibitory effects of human leukocyte IFN up to concentrations of 10,000 units/ml, suggesting that this tumor cell line does not retain antiviral IFN response pathways (**Figure 1e**, right panel). These data illustrate the IFN antagonizing ability of MV[vac2]NIS and highlight its potential use for treatment of tumors retaining functional IFN pathways.

MV[vac2]NIS induces tumor regression and efficient isotope uptake in MCL xenografts

We then implanted Granta-519 xenografts in SCID mice and tested the oncolytic efficacy of MV[vac2]NIS *in vivo*. We administered virus after 20 days of subcutaneous tumor growth, at which point the primary tumors averaged ~500 mm^3 and a small percentage of animals had developed palpable metastatic tumors in the ipsilateral inguinal lymph node. MV[vac2]NIS or vehicle was administered in a single injection, either intratumorally (IT) or intravenously (IV) via the tail vein. All vehicle-treated animals succumbed to advanced tumor burden (>1,500 mm^3) within 2 weeks of vehicle therapy (**Figure 2a**, left panel). In contrast, mice treated with either IV or IT MV[vac2]NIS underwent tumor regression, with the majority of animals achieving complete responses for both primary and metastatic tumors (**Figure 2a**, middle and right panels, respectively).

To understand the mechanisms of oncolysis, we took advantage of the *NIS* transgene. To visualize virus replication, we imaged animals 1 hour after intraperitoneal injection of 500 μCi of pertechnetate. Using the GammaMedica X-SPECT/CT system (GammaMedica Ideas, Northridge, CA), we observed NIS-mediated pertechnetate uptake within the primary tumors by day 5 after IV therapy, with uptake plateauing during the second week
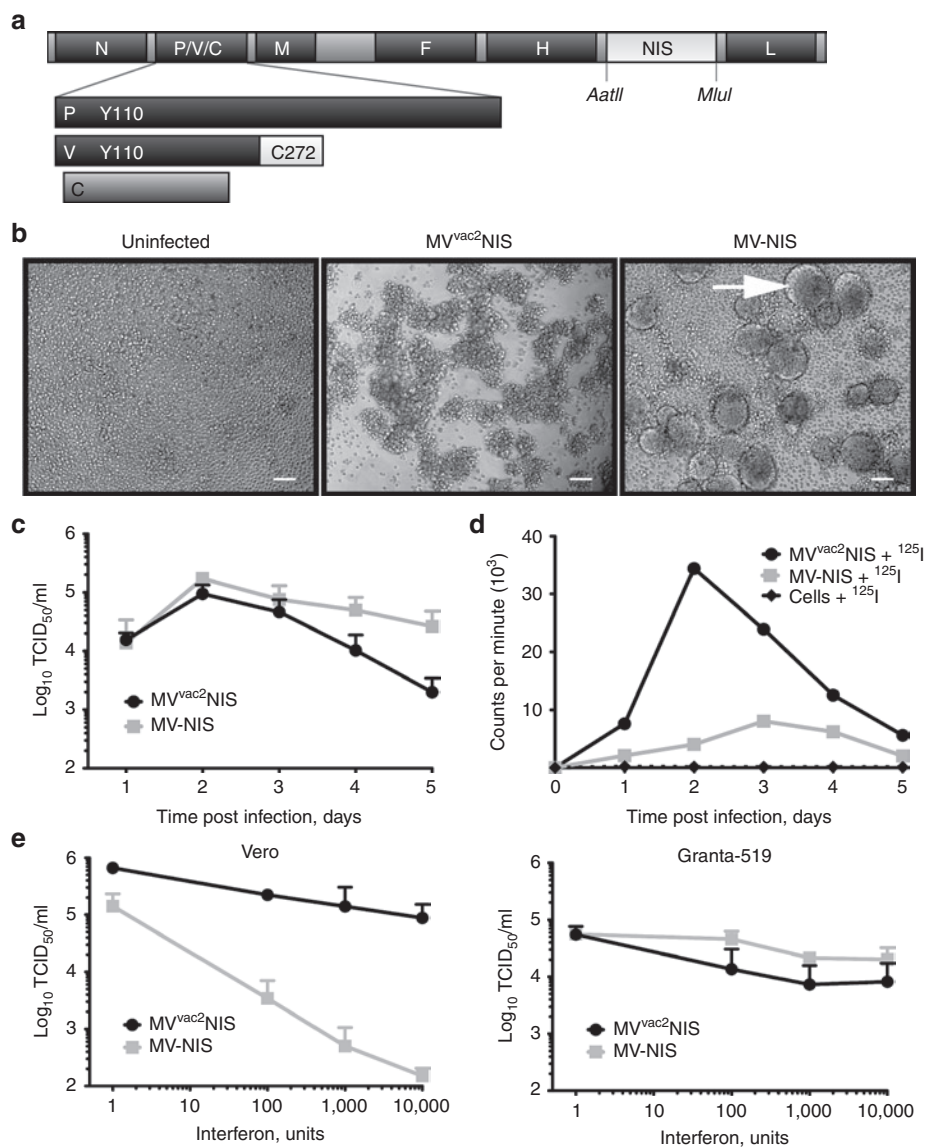
Figure 1 MV^{vac2}NIS efficiently expresses functional NIS within infected MCL cells, and can overcome interferon signaling. (a) Map of the p(+) MV^{vac2}NIS plasmid coding for the MV^{vac2}NIS genome. The human *NIS* gene was inserted in an additional transcription unit downstream of MV-H. The *AatII* and *MluI* restriction sites are indicated. Residues in the P and V proteins important for antagonizing cellular interferon responses are indicated. **(b)** Light microscopy images of Granta-519 cells, uninfected (left) or infected with MV^{vac2}NIS (center) or MV-NIS (right) at 48 hours after infection at a multiplicity of infection (MOI) of 0.03. Scale bars = 5 μm. **(c)** Virus titer for MV^{vac2}NIS and MV-NIS recovered from cell-associated fraction following Granta-519 infection at an MOI of 0.03. Data are given as mean ± SD; *n* = 3. **(d)** Intracellular uptake of ^{125}I by Granta-519 cells infected or not with MV^{vac2}NIS or MV-NIS at an MOI of 0.03. Representative experiment. **(e)** Quantification of virus titer after MV^{vac2}NIS or MV-NIS infections in the presence of increasing concentrations of human leukocyte interferon in Vero (left, 24 hours after infection) and Granta-519 (right, 48 hours after infection) cells. Data are given as mean ± SD; *n* = 3. MCL, mantle cell lymphoma; MV, measles virus.

after virotherapy (**Figure 2b**, center; **Figure 2c**, days 5, 8, and 11). We used SPECT/CT overlay images, as shown in **Figure 2c**, to measure the efficiency of isotope uptake. For each primary tumor, we quantified the percentage of injected pertechnetate dose concentrated per cubic centimeter of tumor tissue (% ID/cc), which was significantly above background between days 5 and 16 for both IV and IT treatment groups (**Figure 2b**; *P* < 0.001 and *P* < 0.01, respectively). We also documented isotope concentration in the smaller, inguinal metastases. A representative metastatic tumor following MV^{vac2}NIS IV therapy is shown in **Figure 2d** as both CT alone (upper panels) and SPECT/CT overlay (lower

panels). This metastatic tumor rapidly reached peak pertechnetate uptake by day 5 after virotherapy and completely regressed by day 16 after virotherapy. However, due to insufficient resolution uptake could not be quantified.

We then compared virus spread after IT or IV administration. IT therapy resulted in less consistent tumor regression (**Figure 2a** right panel), which correlated with less uniform pertechnetate uptake in primary tumors (**Figure 2b** right panel) compared with IV therapy (**Figure 2a,b** middle panels). Despite nearly all animals achieving complete regression of primary and metastatic tumors, all MV^{vac2}NIS-treated animals succumbed to systemic disease
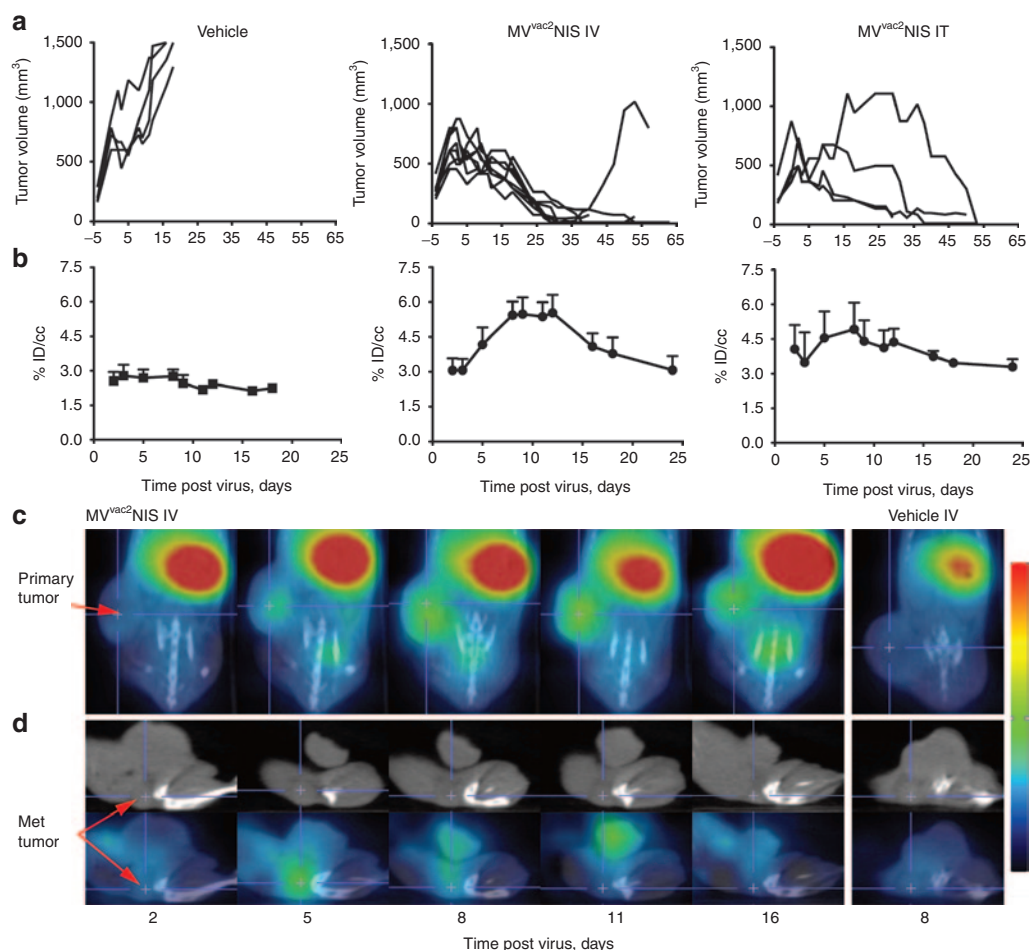
Figure 2 MV^{vac2}NIS replication induces xenograft regression and can be visualized and quantified by SPECT/CT imaging. (**a**) Tumor-response curves for individual animals treated with vehicle or MV^{vac2}NIS IV or IT. (**b**) Uptake of pertechnatate within primary tumors for animals treated with vehicle or MV^{vac2}NIS IV or IT, quantified as the percentage of injected isotope dose concentrated per cubic centimeter of tumor tissue (% ID/cc). Data from same animals as displayed in **a**. Data are given as mean ± SD; $n = 4$ (vehicle), $n = 8$ (IV), $n = 4$ (IT). (**c**) X-SPECT/CT overlay images in coronal plane from representative animals treated with MV^{vac2}NIS IV or vehicle. Primary tumor is indicated. (**d**) CT (upper) and SPECT/CT overlay (lower) images in the sagittal plane from representative animals treated with IV MV^{vac2}NIS or vehicle. Metastatic tumor is indicated. IT, intratumorally; IV, intravenously; MV, measles virus; SPECT, single photon emission computed tomography.

(**Figure 3**). The median survival for IV-treated animals was 74.5 days after tumor implantation ($P < 0.001$), and the causes of death included metastatic MCL disease to the gastrointestinal tract and central nervous system manifesting as ascites and rear limb paralysis, respectively (**Figure 3**, right side). IV and IT therapies resulted in equivalent survival (**Figure 3**, $P = 0.347$) despite IV therapy achieving more uniform tumor regression and efficient pertechnetate uptake. These data suggest that systemic administration delivers virus to perfused, viable tumor tissue more efficiently than local administration does, favoring more consistent isotope uptake and tumor regression.

MV^{vac2}NIS spreads in well-perfused tumor tissue

To characterize the mechanisms resulting in tumor regression, we sought to document viral seeding and spread within infected xenografts. Toward this goal, we used three complementary approaches: autoradiography to visualize virus replication at the cellular level in resected tumors, analysis of Hoechst dye tissue distribution following IV administration as a measure of tissue

perfusion, and a newly available *in vivo* U-SPECTII/CT imaging system allowing high-resolution analysis of virus replication in living tissue.

Figure 4a documents autoradiography of NIS expression (left) and immunohistochemistry for MV-N protein (right) from the same tumor section following IV MV^{vac2}NIS and pertechnetate administration. There is a clear correlation between the location of functional NIS protein (**Figure 4a** left panel, black areas) and the location of the MV-N protein (**Figure 4a** right panel, brown areas). We then documented by autoradiography virus spread in primary tumors sectioned at 500-micron intervals. In a tumor collected 2 days after infection, we observed individual small foci of isotope accumulation indicating virus seeding events (**Figure 4b**, left panel). In primary tumors collected 5, 8, or 12 days after infection, we observed stronger MV^{vac2}NIS infection, accompanied by a shift in the location of infectious centers to the tumor periphery (**Figure 4b**).

We also analyzed metastases collected from mice treated with IV MV^{vac2}NIS. These sections are shown in columns to the right of
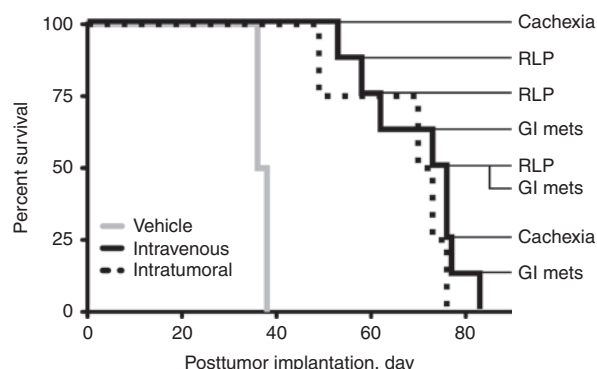
Figure 3 MV^vac2NIS improves survival after both IV and IT administration but is not curative. Kaplan–Meier survival curves for animals treated with vehicle or MV^vac2NIS using IV or IT routes of administration. The causes of death and day of death after tumor implantation are indicated for the MV^vac2NIS IV treatment group. GI Mets, gastrointestinal metastases; IT, intratumorally; IV, intravenously; MV, measles virus; RLP, rear limb paralysis.

the primary sections (**Figure 4b**). In contrast to primary tumors, metastases showed widespread infection covering nearly their entire surface area already at 5 days after virotherapy (**Figure 4b**). To compare isotope uptake within primary tumors and metastases, we measured the percentage of injected pertechnetate dose concentrated per gram of tissue (% ID/g; **Figure 4b**, red values below each set of sections). Uptake in primary tumors peaked around 7–8% ID/g at day 8 and 12 after virotherapy, whereas in metastases, 18–30% ID/g was measured at days 5, 8, and 12 (**Figure 4b**). Thus, MV^vac2NIS spread is more rapid and efficient in metastatic tissue than in primary tumors in the Granta-519 xenograft model.

We also sought to document the changing distribution of infections over time. Toward comparing spread in internal versus peripheral areas, we defined outer (O), middle (M), and inner (I) concentric regions for each primary tumor section, and then applied a pixel threshold based on background analyses of control tumors. The number of pixels above this threshold was measured within each concentric region. At day 2, we observed only small areas of infection evenly distributed in the O, M, and I regions, indicating homogenous seeding events throughout tumors (**Figure 4c**, upper graph, and lower top panel). At later time points, infection was much more extensive within the outermost region than within the two inner regions (**Figure 4c**, upper graph, and lower bottom panel).

We then asked whether virus replication at the late time point would correlate with perfused, viable tissue. To visualize perfused tissue, we injected IV Hoechst dye 10 minutes before killing and tumor harvest.[30,31] In the interior of the tumors, infection and perfusion were rare. Conversely, nearly all regions of perfusion showed active virus replication (**Figure 4d**, compare top left and top right panels, white arrows), although certain uninfected nodules could be observed (**Figure 4d**, nodule indicated with red arrow). On H&E staining, Hoechst dye and virus infection correlated closely with lymphocyte-dense regions of tumors staining with hematoxylin, whereas regions lacking Hoechst dye and infection stained strongly eosinophilic, suggestive of necrosis (**Figure 4d**, bottom panel). Furthermore, when comparing primary

and metastatic tumors from the same animal, we observed highly variable and compromised perfusion of primary tumors even at day 2 after virotherapy, whereas metastases had more consistent and widespread distribution of Hoechst dye (**Figure 4e**, compare left and right panels). Altogether, these observations suggest that MV^vac2NIS infection is seeded homogenously in tumors, but only the peripheral, well-perfused regions of the primary tumors, as well as the whole of metastases, support efficient viral replication.

Kinetic analysis of virus spread in tumors of living hosts

We correlated virus amplification with areas of tumor perfusion based on comparisons of tumors harvested from different animals. Ideally, kinetic analysis of virus spread should be performed in living animals, but until recently available systems did not achieve sufficient resolution. However, a new U-SPECTII/CT system provides *in vivo* resolution capable of aligning infectious centers in three dimensions as they evolve and spread over time. Thus, we can now obtain 3D kinetic analysis of virus spread in tumors of living hosts.

Figure 5a displays a U-SPECTII/CT overlay analysis in the coronal, transverse and sagittal planes following IV MV^vac2NIS virotherapy in an individual animal. To standardize serial images, the base of primary tumors was aligned vertically in both coronal and transverse axes, generating a sagittal cross section equivalent to tumor autoradiography analysis (**Figure 5a**). This process is illustrated in **Figure 5b**, which displays the tumor of one animal visualized by U-SPECTII/CT imaging (left panel) and then resected and analyzed by autoradiography (right panel). Thus, data obtained *in vivo* by noninvasive imaging correlate well with data obtained after tumor harvest. Moreover, U-SPECTII/CT retains a wide dynamic range for visualizing the relative intensity of infection within individual foci (**Figure 5b**, left panel).

Figure 5c shows a representative analysis of the intratumoral spread of an oncolytic vector in three-dimensions over time. Optical sections from infected primary (top) and metastatic (bottom) tumors present in the same animal are displayed based on their relative tumor depths in the sagittal plane. For this primary tumor, we visualized the infection progress from small foci at day 4 to a complete ring around the outer region of the tumor by day 9 after virotherapy. The metastatic tumor from the same animal (**Figure 5c** bottom) shows an earlier and more intense infection peak at day 4, with complete resolution by day 11 after virotherapy. Complete SPECT/CT tomographic analyses and 3D reconstructions from day 9 after virotherapy are available for the animal in **Figure 5c** as **Supplementary Videos S1–S4**.

Greater U-SPECTII/CT resolution allowed quantification of isotope uptake in the metastatic tumors, as well as in the thyroid, which is usually difficult to define due to proximity to the NIS-expressing salivary glands. The average uptake in metastases was higher than that of primary tumors as quantified by U-SPECTII/CT on days 4 and 7 after virotherapy (**Figure 5d**, $P < 0.0001$, $P < 0.05$, respectively). We calculated an average of ~20% ID/cc isotope uptake in metastatic tumors at peak MV^vac2NIS infection (**Figure 5e**). Pharmacologically blocked thyroid uptake averaged 55% ID/cc, about 2.75-fold higher than the peak uptake observed in the metastatic tumors ($P < 0.001$), whereas
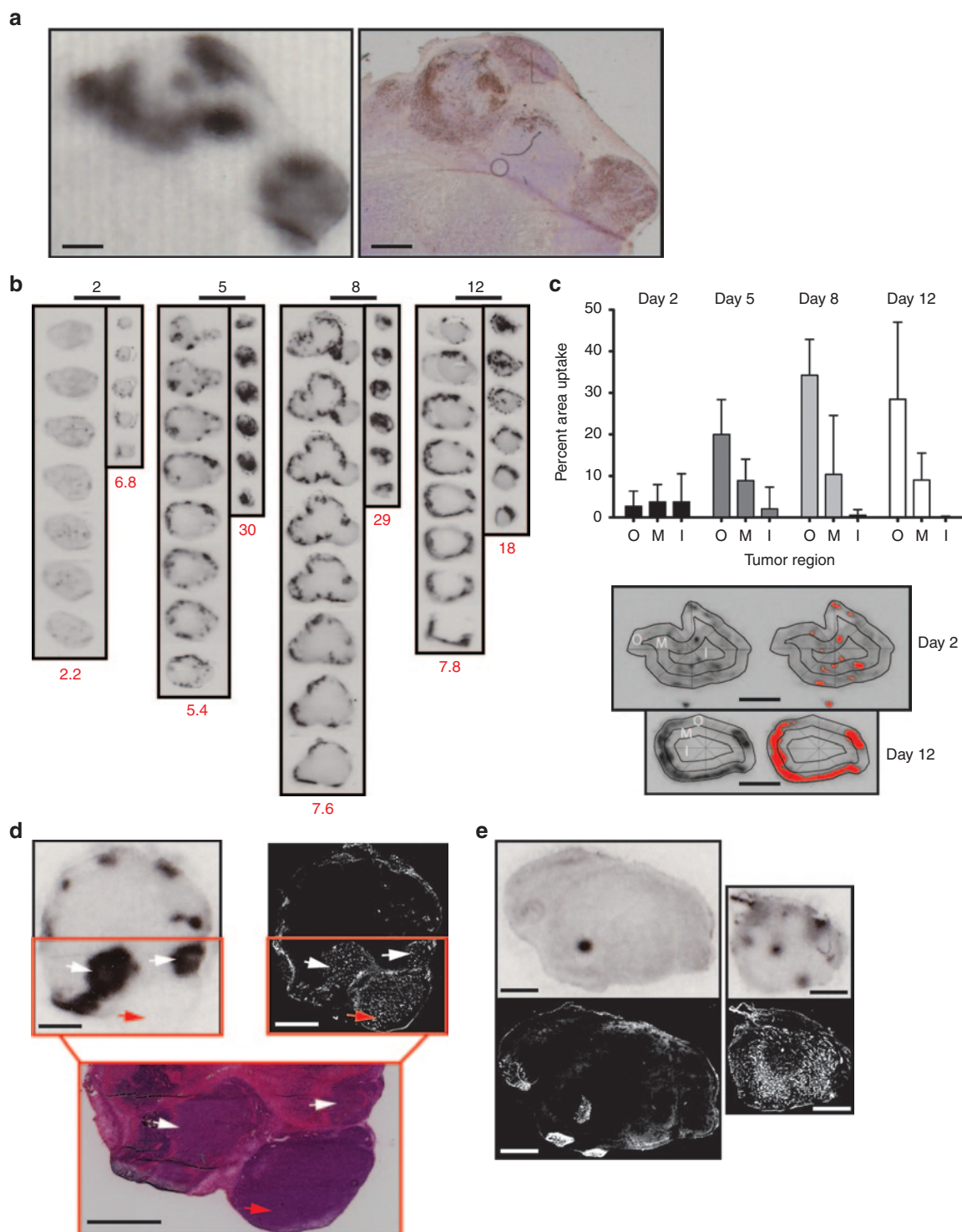
Figure 4 **High-resolution *ex vivo* imaging correlates virus replication with tumor perfusion over time.** (**a**) Autoradiography (left) of functional NIS expression and immunohistochemistry (right) for MV-N antigen on the same tumor section. Scale bars = 1 mm. (**b**) Autoradiography of serial sections taken at 500 µmol/l intervals from primary and metastatic tumors collected at different times after infection. Quantification of the percentage injected dose of pertechnetate concentrated per gram of tissue (% ID/g) for each tumor is indicated in red at the bottom of each column. Scale bars above each column = 10 mm. (**c**) Localization of virus infection within harvested primary tumors (top panel) and examples of the concentric (O, outer; M, middle; I, inner) and threshold masks (bottom panel) applied to digitized images of each tumor section. Error bars indicate mean ± SD; $n = 13$ (Day 2), $n = 17$ (Day 5), $n = 18$ (Day 8), $n = 18$ (Day 12). Scale bars = 5 mm. (**d**) Primary tumor section obtained 12 days after IV inoculation of MV^{vac2}NIS analyzed first by autoradiography (top left), then by Hoechst fluorescence (top right), and finally by H&E staining (bottom). Infected, perfused, and viable regions of the tumor are indicated by white arrows; a perfused, viable but uninfected region of tumor is indicated by one red arrow. Scale bars = 2 mm. (**e**) Comparison of primary (left) and metastatic (right) tumors from the same animal analyzed by autoradiography (top panels) and Hoechst staining (bottom panels) at day 2 after infection. Scale bars = 2 mm. IV, intravenously; MV, measles virus.
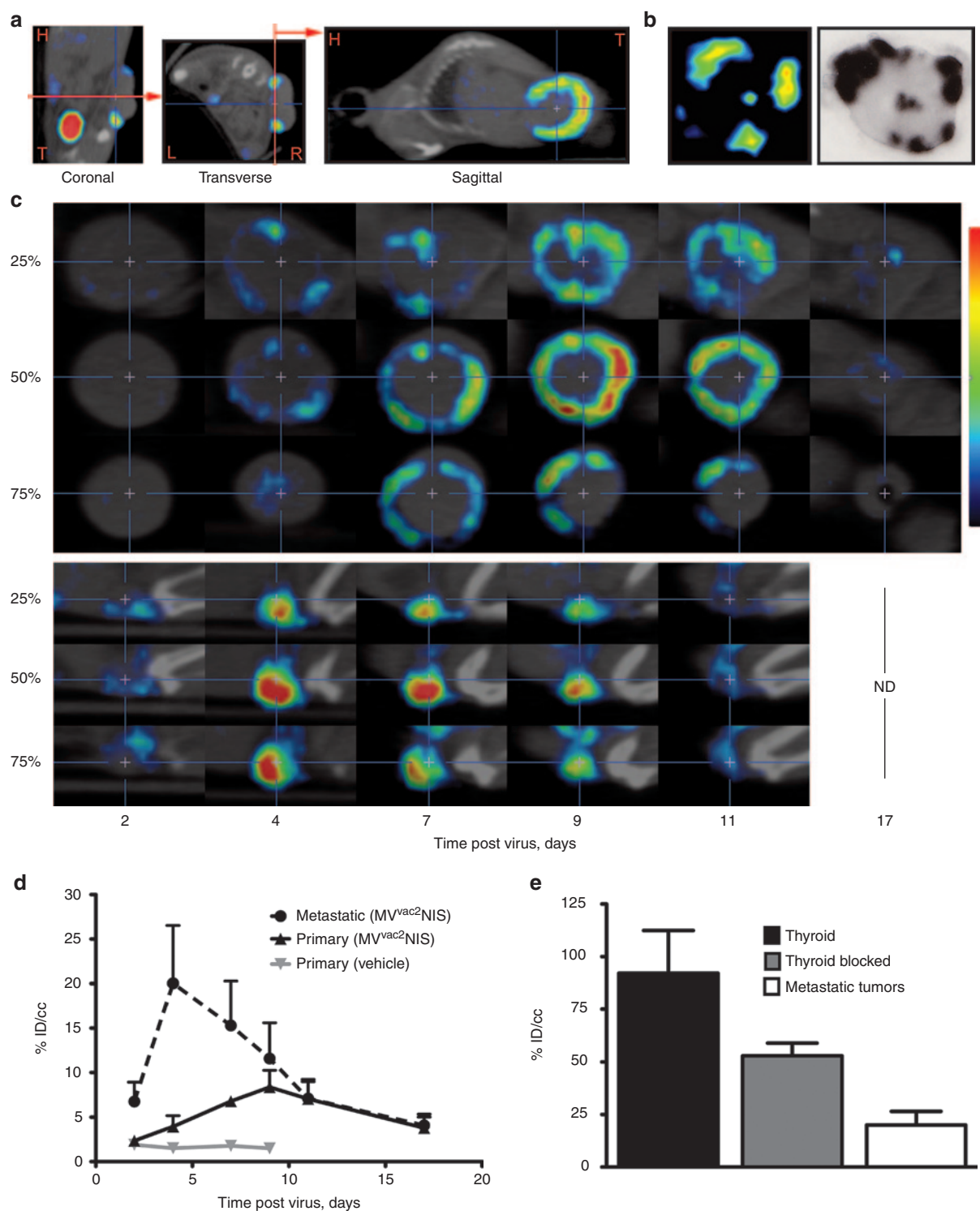
Figure 5 High-resolution SPECT/CT quantifies virus infection in primary and metastatic tumors from the same animal. (**a**) Image analysis following U-SPECTII/CT imaging, illustrating vertical alignment of primary tumor bases in the coronal and transverse planes to obtain autoradiography-equivalent images from the sagittal plane. H, head; T, tail; L, left; R, right. (**b**) Comparison of an individual primary tumor analyzed first by U-SPECTII/CT and subsequently harvested and analyzed by autoradiography. (**c**) Serial images in the sagittal plane of a primary tumor (top) and metastatic tumor (bottom) from the same animal at multiple time points following IV administration of MV^{vac2}NIS. Images from different depths within the same tumor are shown; the relative position of each image within the total tumor depth is indicated on the left. (**d**) Quantification of isotope uptake within primary and metastatic tumors from the same animals at multiple time points after MV^{vac2}NIS IV administration. Data are given as mean ± SD; $n = 5$ (MV^{vac2}NIS, metastatic and primary), $n = 1$ (vehicle). (**e**) Comparison of pertechnetate uptake within murine thyroid pharmacologically blocked or not with L-thyroxine and peak metastatic tumor uptake on day 4 after infection with IV MV^{vac2}NIS. Data are given as mean ± SD; $n = 5$ (metastatic tumor), $n = 6$ (blocked thyroid), $n = 2$ (thyroid). IV, intravenously; MV, measles virus; SPECT, single photon emission computed tomography.
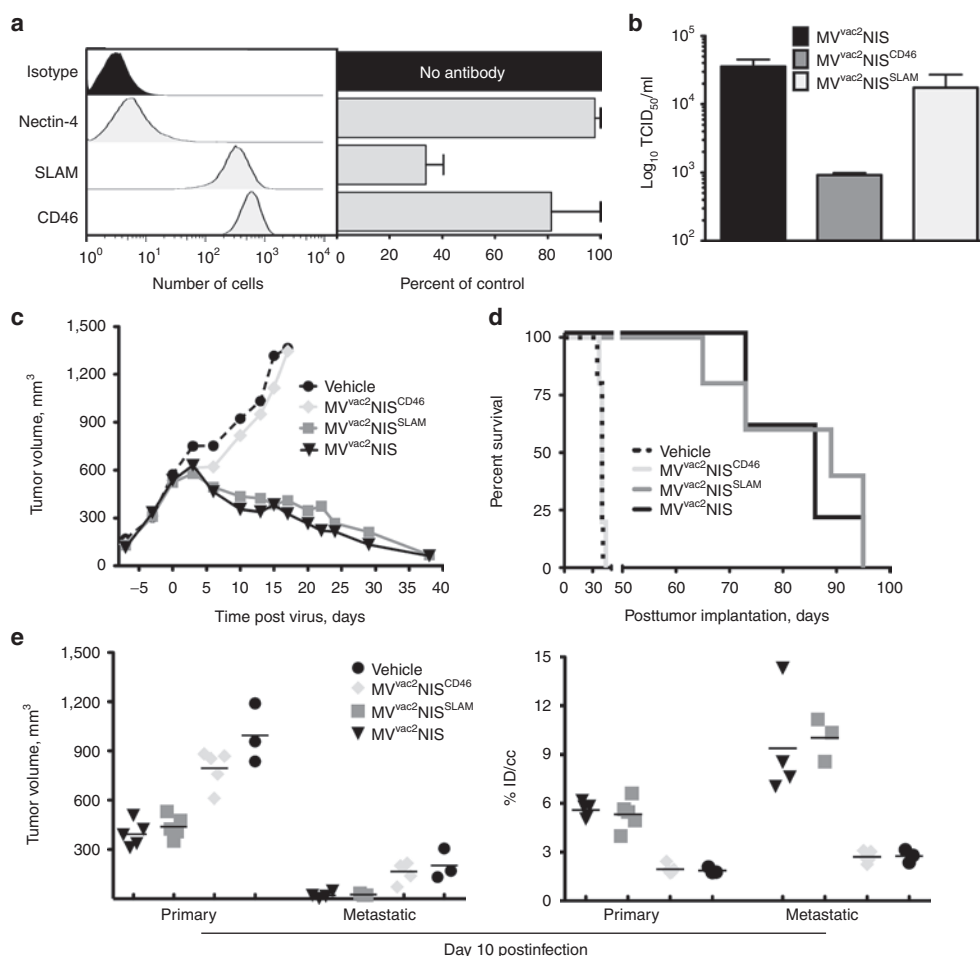
Figure 6 Cell entry through SLAM but not CD46 sustains efficient MV^{vac2}NIS oncolysis. (**a**) Flow cytometry analysis of surface expression of MV receptors nectin-4, CD46, and SLAM on Granta-519 cells (left, representative experiment) and the effects of receptor-blocking antibodies on MV^{vac2}GFP infection of Granta-519 cells *in vitro*, as measured by flow cytometry for GFP^{+} cells (right, data are given as mean ± SD; $n = 3$). (**b**) Cell-associated virus titers for MV^{vac2}NIS, MV^{vac2}NIS^{CD46}, and MV^{vac2}NIS^{SLAM} 48 hours after infection at an multiplicity of infection (MOI) of 0.03 in Granta-519 cells. Data are given as mean ± SD; $n = 3$. (**c**) Mean tumor response curves, as measured externally with calipers, for animals treated with IV vehicle or the three viruses indicated. Data points represent means ($n = 5$), error bars were excluded for clarity. (**d**) Kaplan–Meier survival curve for animals treated IV with vehicle or the three viruses indicated. (**e**) U-SPECTII/CT quantification of tumor volume (left) and isotope uptake (right) within primary and metastatic tumors 10 days after IV administration of vehicle or the three viruses indicated. Data points represent individual tumors, lines indicate means. **c–e** display data from a single experiment. IV, intravenously; MV, measles virus; SPECT, single photon emission computed tomography.

nonmedicated thyroid uptake was higher than both metastatic tumors and blocked thyroid ($P < 0.001$), approaching 90% ID/cc. These data indicate that MV^{vac2}NIS can induce isotope uptake in metastatic tumors within approximately threefold the efficiency of thyroid tissue. Of note, the U-SPECTII/CT quantification of isotope uptake per cubic centimeter for primary and metastatic tumors agrees closely with the isotope uptake quantification from harvested tumors measured per gram of tissue (**Figure 4b**, red values). In summary, U-SPECTII/CT imaging documented and quantified the different kinetics, intensities, and distributions of MV^{vac2}NIS infection within primary tumors and metastases from the same animal.

SLAM is the dominant oncolytic MV receptor in MCL
We then used this novel imaging technology to characterize the viral entry pathway supporting productive infection and oncolysis. All MV strains use the immune-cell specific protein SLAM for

entry, and SLAM expression correlates with regression of hematological malignancies after natural MV contagion.[11] Conversely, CD46 overexpression on tumor cells of different origins can also support MV oncolysis.[18,19,32] Finally, nectin-4, which was recently identified as the epithelial receptor for MV,[33,34] is also a tumor cell marker.[35–37] Toward characterizing the relevance of these different entry pathways, we documented the expression of all three MV receptors on Granta-519 cells by fluorescence activated cell sorting. We observed high levels of expression for both SLAM and CD46, whereas nectin-4 expression was not observed (**Figure 6a**, left panel). We then used anti-nectin-4, SLAM, and CD46 antibodies to block *in vitro* infection and differentiate the contributions of each receptor to MV infectivity. We observed that the SLAM antibody reduced infection by about 70%, whereas the CD46 antibody reduced entry by about 20%, and the nectin-4 antibody had only a marginal effect (**Figure 6a**, right panel). We also examined MV^{vac2}NIS growth in three additional MCL cell lines, one that

expresses SLAM (JVM-2) and two that do not (Mino-1, HBL-2; **Supplementary Figure S3**). MV^{vac2}NIS grew efficiently only in the SLAM-expressing JVM-2 cell line.

To directly compare the relevance of the SLAM and CD46 entry pathways, we generated MV^{vac2}NIS vectors selectively recognizing only SLAM (MV^{vac2}NIS^{SLAM}) or only CD46 (MV^{vac2}NIS^{CD46}) by mutating individual amino acids in the viral attachment protein H that sustain either one or the other receptor interaction (see Materials and Methods section). We confirmed receptor specificity of both viruses using cell lines expressing only CD46 (Vero) or only SLAM (CHO-SLAM; **Supplementary Figure S4**). We then infected Granta-519 cultures *in vitro* with these viruses, observing MV^{vac2}NIS^{SLAM} titers only slightly lower than MV^{vac2}NIS, whereas MV^{vac2}NIS^{CD46} replicated to about 30 times lower titers (**Figure 6b**). This is consistent with receptor-blocking antibody data and suggests preferential usage of SLAM over CD46 by MV^{vac2}NIS *in vitro*.

We next treated Granta-519 xenografts with the receptor-specific vectors, and quantified their replication in primary and metastatic tumors by U-SPECTII/CT imaging. The results were clear-cut: MV^{vac2}NIS^{SLAM}-induced tumor regression ($P > 0.05$ for all time points) and survival ($P = 0.621$) equivalent to MV^{vac2}NIS, whereas virotherapy with MV^{vac2}NIS^{CD46} was equivalent to vehicle treatment and unable to control tumor growth ($P > 0.05$ for all time points) or extend survival (**Figure 6c,d**; $P = 0.608$). On day 10 after virotherapy, we quantified by U-SPECTII/CT imaging tumor volume and isotope uptake for primary tumors and metastases (**Figure 6e**, left and right panels, respectively). MV^{vac2}NIS^{SLAM} elicited tumor regression and isotope uptake equivalent to parental MV^{vac2}NIS for both primary and metastatic tumors ($P > 0.05$), whereas MV^{vac2}NIS^{CD46} treatment was equivalent to vehicle treatment for both tumor growth and isotope uptake at both sites ($P > 0.05$). Thus, MV^{vac2}NIS infection and spread within MCL xenografts is completely dependent on SLAM expression.

Radiovirotherapy can cure nude mice of MCL xenografts

In an effort to enhance therapeutic efficacy, we combined MV^{vac2}NIS virotherapy with the high-energy radioisotope ^{131}I to induce bystander tumor killing. Due to the pronounced radiosensitivity of SCID mice,[38] we tested this combination regimen in the more radio-tolerant athymic nude strain. We administered radioiodine by intraperitoneal injection 15 days after starting virotherapy, based on imaging studies indicating a plateau of isotope uptake at this time point in the nude mouse xenograft model (**Supplementary Figure S5**).

Mice receiving MV^{vac2}NIS showed minimal responses to virus alone for ~10 days after treatment, with tumor volumes increasing in parallel for virotherapy groups and the group receiving only vehicle (**Figure 7a**). Notably, in the days following systemic administration of 1 mCi of ^{131}I, an accelerated and consistent regression of tumors occurred in the combination therapy group, whereas in the virus-only group, therapeutic effects were less pronounced (**Figure 7a,b**). However, due to tumor variability within treatment groups, the combination therapy was not significantly better than virus alone for inducing tumor regression ($P > 0.05$

for all time points after ^{131}I administration). Isotope treatment in the control group had no observable effect on tumor growth (**Figure 7a**), indicating that enhanced tumor regression in the combination therapy group was due to localized concentration of ^{131}I within MV^{vac2}NIS-infected cells inducing bystander cell killing. Granta-519 xenograft implantation in nude mice did not cause systemic disease, and most animals receiving either virotherapy or radiovirotherapy displayed full remission (**Figure 7c**). Altogether, our data indicate that NIS-mediated radiovirotherapy can efficiently concentrate radiation specifically within tumor tissue, an important property when treating diseases like MCL that are radiosensitive but spread systemically.
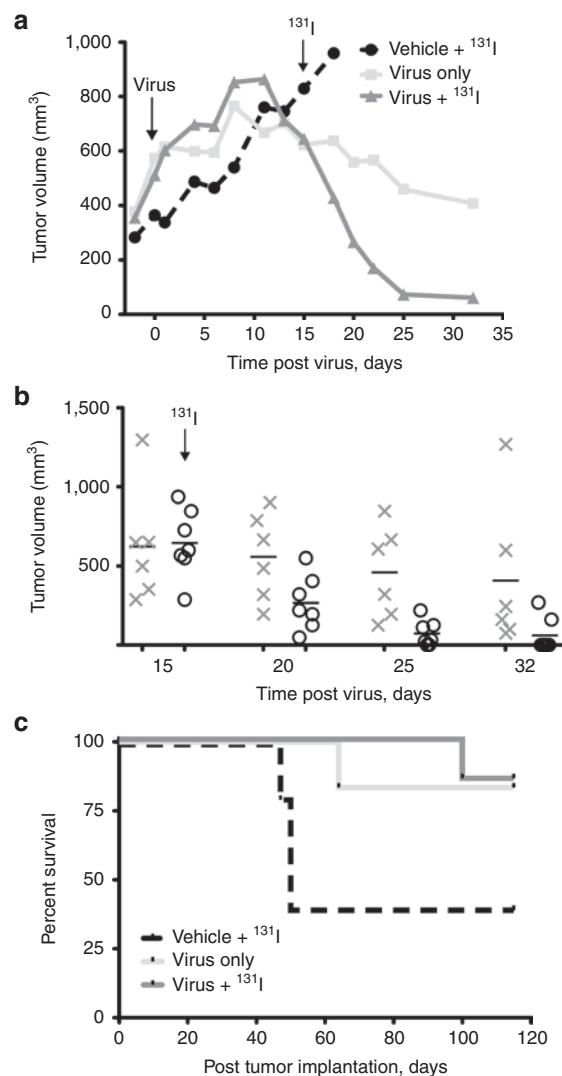

Figure 7 Radiovirotherapy can be curative. (**a**) Tumor-response curves for animals treated IV with MV^{vac2}NIS or vehicle, and then treated or not with 1 mCi ^{131}I administered by intraperitoneal (IP) injection, as indicated. Data points represent means; error bars were excluded for clarity. (**b**) Individual data points are shown for days 15, 20, 25, and 32 after virus administration for animals treated with virus alone (gray X) or combination virus plus ^{131}I (black circles). (**c**) Kaplan–Meier survival curves for animals treated with MV^{vac2}NIS ($n = 6$), MV^{vac2}NIS + ^{131}I ($n = 7$), or vehicle + ^{131}I ($n = 5$). IV, intravenously; MV, measles virus.

DISCUSSION

Case reports suggest that in hematological tumors expressing SLAM, wild-type MV spread following natural contagion can be so robust as to cause remission.[13,14] We show here using high-resolution–computed tomography imaging and autoradiography that a vaccine-identical MV vector expressing NIS can spread rapidly through perfused tumor tissue and cause regression of primary MCL xenografts and metastases. We also developed a radiovirotherapy regimen that concentrates ^{131}I specifically within MV[vac2]NIS-infected xenografts to induce more rapid and consistent tumor regression. Strikingly, efficacy of virotherapy was completely dependent on cell entry through MV's primary receptor SLAM, which is a signaling molecule.

MV is currently used in clinical trials for ovarian cancer[17] (NCT00408590), glioblastoma multiforme (NCT00390299), multiple myeloma (NCT00450814), and mesothelioma (NCT01503177). These trials were developed based on the observation that CD46 overexpression drives preferential infection and destruction of cultured cells and certain xenografts by vaccine-lineage MV.[18,19,32] Analogously, previous preclinical analyses of MV spread in different cancer cell types, including our studies in MCL,[22] were interpreted based on the assumption that cell entry through CD46 or SLAM would sustain MV spread with equivalent efficiency. However, recent studies in macaques showed that the SLAM entry pathway is most relevant in natural hosts: even vaccine MV preferentially infects SLAM-positive immune cells.[20] Moreover, wild-type MV expressing vaccine-strain hemagglutinin maintained the same SLAM-dependent cellular tropism in macaques as wild-type MV.[21] In addition, lentiviruses pseudotyped with the glycoproteins of the MV vaccine strain preferentially transduce B cells expressing high levels of SLAM over T-cells expressing lower levels of SLAM, and induce downregulation of SLAM but not CD46 during infection.[39] These observations and our results suggest that in vivo MV generally exploits the SLAM entry pathway to establish a productive infection in immune cells, while infection of the same cells through CD46 results in blunted replication. This likely reflects an ancient adaptation of viruses in the Morbillivirus genus for rapid and discrete primary spread in SLAM-expressing immune cells.[10] Thus, MV-based oncolysis is most likely to be effective in lymphomas expressing SLAM, which is consistent with the observation that SLAM-positive malignancies can regress following wild-type MV contagion.[13,14] Susceptible tumor types may include diffuse large B-cell lymphoma[40] and Epstein–Barr virus–related lymphoproliferative disease in chronically immunosuppressed individuals.[41] Work is currently underway to characterize the levels of SLAM expression for multiple lymphoma subtypes, and to determine the threshold of SLAM expression necessary to sustain oncolysis in hematologic tumors, which may be lower than defined for CD46[18] because of SLAM redistribution to contact points between immune cells.[42]

Generally, oncolysis may be most efficient in cancer types derived from tissues in which viruses have evolved to replicate at high levels. These tissues include, but are not limited to, those in which viruses cause disease. Wild-type MV also replicates efficiently in airway epithelium, which it accesses through the adherens junction protein nectin-4.[33,34] Remarkably, this protein is frequently expressed in breast,[35] lung,[36] and ovarian cancer,[37] identifying these tumor types as potential targets for MV oncolysis. It will be of future interest to determine if there exists a correlation between nectin-4 expression on ovarian tumors and prolonged survival following MV virotherapy.[17] If so, future clinical trials may focus on patients with nectin-4–driven vulnerability to MV virotherapy.

Tracking MV replication during oncolysis has been implemented in the clinic using both virally encoded soluble CEA and NIS proteins.[17] Using the latter in combination with high-resolution computer tomography, we characterized here the different kinetics, intensities, and distributions of primary and metastatic tumor infections in living hosts for over 2 weeks. We documented efficient vector spread within even small, isolated foci of perfused and viable tumor tissue. A similar strategy using vaccinia virus has recently reported prolonged virus replication in perfused, viable tissue and enhanced efficacy with radiovirotherapy.[43] Our current work advances the resolution of noninvasive imaging to characterize multiple infection foci simultaneously, which in the clinical setting will allow direct correlation of viral replication and spread with clinical measures of efficacy and inform sequential rounds of therapy targeted at disease foci displaying subtherapeutic infection levels. It will also improve safety by allowing timely surveillance of any off-target vector replication.

By combining virotherapy with ^{131}I, high-energy isotope was concentrated specifically within tumor xenografts, mimicking the successful exploitation of NIS expression in metastatic thyroid cancer by systemic ^{131}I therapy. Remarkably, NIS-mediated isotope uptake in infected metastases was within about threefold the efficiency of the thyroid, suggesting a large proportion of tumor cells expressed NIS. Even in primary tumors that concentrated less isotope, combination radiovirotherapy induced more rapid tumor regression than virotherapy or radiotherapy alone. Radiovirotherapy is an especially appropriate therapeutic strategy for MCL, which is susceptible to radiotherapy but spreads systemically before diagnosis and therefore requires more stringent tumor specificity to safely treat with radiation. Additional preclinical dosimetry studies are needed to better characterize the minimum effective dose of ^{131}I in our murine model and correlate it with equivalent doses in humans.

In conclusion, the vaccine-identical MV expressing NIS developed here is a potent oncolytic agent in primary and metastatic MCL xenografts following systemic administration. NIS expression allowed in vivo visualization of viral replication at an unprecedented resolution and quantified viral gene expression in primary tumors and metastases of living hosts over time. In nude mice, radiovirotherapy achieved complete remissions, which were entirely dependent on MV's primary receptor entry pathway. Although virus entry into cells can occur through multiple receptors, the efficacy of oncolytic protocols may depend on the concurrent activation of cellular responses that support efficient viral replication. Functioning as both an entry receptor and signaling molecule, SLAM expression on hematologic tumors represents a targetable vulnerability for MV-based oncolysis in future clinical trials.

MATERIALS AND METHODS

Cells. All cell lines were grown at 37 °C in a humidified atmosphere of 5% CO_2. The human MCL cell line Granta-519[44,45] was grown in RPMI supplemented with 10% fetal calf serum (Invitrogen, Carlsbad, CA) heat inactivated at 56 °C for 30 minutes. The human MCL cell lines JVM-2, HBL-2, and Mino-1 (kindly provided by S Parekh, Albert Einstein Cancer Center, Bronx, NY) were grown in RPMI supplemented with 10% fetal calf serum. Vero cells (African green monkey kidney; CCL-81; ATCC), Vero-hSLAM (kindly provided by Y Yanagi, Kyushu University, Fukuoka, Japan), and CHO-hSLAM cells were grown in Dulbecco's modified Eagle's medium (Mediatech, Herndon, VA) supplemented with 10% fetal calf serum, with 0.5 mg/ml G418 selection applied to Vero-hSLAM and CHO-hSLAM cell lines.

Viruses. MV^{vac2}NIS was generated by excising the human NIS cDNA from p(+)MV-NIS plasmid[5] using *AatII* and *MluI*. This cDNA was cloned in place of green fluorescent protein (GFP) in the additional transcription unit downstream of MV-H in p(+)MV^{vac2}GFP[24,26] using *AatII* and *MluI* restriction sites. MV^{vac2}NIS coding for either Y481A (MV^{vac2}NIS^{SLAM}, forward primer: CCGAGATTCAAGGTTAGTCCCGCACTCTTCACTGTCCCAATT AAGG, reverse primer: CCTTAATTGGGACAGTGAAGAGTGCGGG ACTAACCTTGAATCTCGG) or R533A (MV^{vac2}NIS^{CD46}, forward primer: GCAACCTACGATACTTCCGCGGTTGAACATGCTGTGGTTTATT ACG, reverse primer: CGTAATAAACCACAGCATGTTCAACCGCGG AAGTATCGTAGGTTGC) were generated by subcloning the *H* gene of MV^{vac2}NIS using *PacI* and *SpeI* double digest to generate the expression plasmid pCG-Vac2-H. Site-directed mutagenesis using *Pfu Ultra II* polymerase (Agilent Technologies, Santa Clara, CA) was used to generate mutants, followed by cloning of the mutant *H* genes back into p(+)MV^{vac}-^{2}NIS using *PacI* and *SpeI* sites. The correct sequences of all constructs were confirmed by sequencing (ABI Prism 337 DNA sequencer; Perkin-Elmer Applied Biosystem, Foster City, CA). p(+)MV-NIS was kindly provided by D Dingli (Mayo Clinic, Rochester, MN). Recombinant viruses were generated using the MV reverse genetics system as previously described,[27] with rescue cells overlaid on Vero-hSLAM (MV^{vac2}NIS, MV^{vac2}NIS^{SLAM}, MV-NIS) or Vero (MV^{vac2}NIS^{CD46}) cells for clone isolation. To generate stocks, viruses were inoculated at multiplicity of infection (MOI) of 0.03 on Vero or Vero-hSLAM monolayers at 32 °C. Cells were scraped in Opti-MEM (Gibco, Carlsbad, CA), particles released using two freeze-thaw cycles in liquid nitrogen and centrifuged at 1,950g for 15 minutes at 4 °C. Titers were determined by 50% endpoint titration on Vero or Vero-hSLAM cells according to the Spearman-Kärber method.[46,47]

In vitro studies. For all *in vitro* studies, cell lines were infected at an MOI of 0.03 in Opti-MEM for 2 hours at 37 °C with gentle shaking every 30 minutes. After incubation, free virus was removed and cells resuspended in fresh growth media. For imaging cytopathic effect in Granta-519 cells, cultures were photographed at 48 hours after infection using a 10X objective. Cytotoxicity was determined using the Cell Proliferation Kit I (Roche, Indianapolis, IN) as per manufacture's recommendations. Cell viability was calculated as the mean of triplicate optical density values, divided by the mean triplicate optical density value of uninfected Granta-519 cultures and expressed as a percentage of control.

For kinetics analysis of virus growth, 5×10^5-infected Granta-519, JVM-2, HBL-2, and Mino-1 cells were seeded in 12-well plates. Individual wells were harvested daily for 5 days. Cells and supernatant (1 ml) were centrifuged at 5,000 rpm for 5 minutes, and supernatant was removed and saved. The cell pellet was resuspended in 1 ml of fresh growth media and subjected to two freeze-thaw cycles using liquid N_2. Cell and supernatant viral titers were determined in duplicate for each sample on Vero-hSLAM cells as described above.

To analyze isotope uptake, 5×10^5-infected Vero and Granta-519 cells were seeded in 12-well plates. At each time point, one well of cells was washed with warm HBSS (Mediatech, Manassas, VA), and then resuspended in warm HBSS with 10 mmol/l Hepes pH 7.3 containing 1×10^6 counts per minute of ^{125}I and 10 µmol/l NaI. Reactions were incubated for 50 minutes at 37 °C, and then washed with cold 10 mmol/l Hepes pH 7.3. Cells were resuspended in 1 N NaOH and mixed by pipetting. Resultant cell lysates were quantified for counts per minute of ^{125}I activity using a gamma counter.

Infected monolayers were visualized by incubating with naphthol blue black for 30 minutes. Cytotoxicity was determined using the Cell Proliferation Kit I (Roche) as per manufacture's recommendations. For NIS expression, we immunoblotted with an anti-NIS antibody (1:50,000 dilution) kindly provided by J Morris[48] as previously described.[49] Cell viability was calculated as the mean of triplicate optical density values, divided by the mean triplicate optical density value of uninfected Granta-519 cultures and expressed as a percentage of control, as previously described.[50]

For IFN studies, 5×10^5 Granta-519 cells and 4×10^5 Vero cells were infected in Opti-MEM for 2 hours at an MOI of 0.03, after which free virus was removed and cells were resuspended in fresh growth media containing different concentrations of IFN from human leukocytes (Sigma-Aldrich, St Louis, MO). At 24 hours after infection, supernatant was removed from Vero cultures, cells were scraped in 1 ml of fresh growth media, and then subjected to two rounds of freeze-thaw. At 48 hours after infection, Granta-519 cells were centrifuged and the supernatant was removed. Cells were resuspended in 1 ml of fresh growth media and subjected to two rounds of freeze-thaw. Samples were titered in duplicate as described above.

For FACS analysis, cells were washed three times with phosphate-buffered saline (PBS), and then resuspended in wash buffer (1× PBS, 5% fetal calf serum, 0.1% NaN$_3$) containing 2 µg of primary antibody (M177 mouse anti-CD46, kind gift from T Seya; N4.61 mouse anti-nectin-4, kind gift from M Lopez; IPO-3 mouse anti-SLAM, Abcam, Cambridge, MA; and isotype control mouse IgG2a, BD Biosciences, San Jose, CA). Following a 1-hour incubation on ice, cells were washed three times in wash buffer, and resuspended in wash buffer containing 2 µl of phycoerythrin (PE)-conjugated anti-mouse secondary antibody (115-116-146; Jackson Laboratories, West Grove, PA). Following a 1-hour incubation on ice, cells were washed three times with wash buffer before FACS analysis. For antibody blocking experiments, MV^{vac2}GFP (MOI of 0.03) and 5 µg antibody were added together to cells in a small volume of growth media and incubated for 2 hours with shaking every 30 minutes. Following incubation, additional growth media was added and cultures were plated and incubated for an additional 36 hours. Following incubation, cells were washed twice in FACS wash solution and resuspended in 4% paraformaldehyde for 24 hours before FACS analysis for GFP$^+$ cells.

Immunohistochemistry. Following autoradiography and Hoechst analysis, slides were fixed for 10 minutes in −20 °C methanol and allowed to air dry. All immunohistochemistry steps were performed at room temperature. Tissue sections were permeabilized with PBS 0.01% Triton X-100 for 10 minutes. H_2O_2 (0.3% vol/vol) was used to quench endogenous peroxidase activity, and sections were washed twice with tris-buffered saline. Sections were blocked with Protein Block solution (NovoLink Min Polymer Detection System, Leica Biosystems, Wetzlar, Germany) for 5 minutes, followed by incubation with a 1:100 dilution of anti-MV-N monoclonal antibody (MAB8906; Chemicon, Billerica, MA) in PBS for 1 hour. Sections were washed twice in tris-buffered saline, and then incubated with Post Primary Block solution (NovoLink Min Polymer Detection System, Leica Biosystems) for 30 minutes. Sections were washed twice with tris-buffered saline, and then incubated with NovoLink Polymer solution for 30 minutes, followed by two more tris-buffered saline washes with gentle rocking. Sections were developed using a 5-minute incubation in DAB working solution (NovoLink Min Polymer Detection System, Leica Biosystems) followed by a water rinse to stop the reaction. Sections were counterstained with hematoxylin for 1 minute rinsed with water and allowed to

air dry before permanent mounting (VectaMount, Vector Laboratories, Burlingame, CA). Slides were visualized using an Axioplan 2 light microscope (Carl Zeiss Microscopy, Jena, Germany) with a 20X objective.

Granta-519 xenograft model. All animal studies were approved by the Mayo Institutional Animal Care and Use Committee. SCID and athymic nude mice were purchased from Harlan Laboratories (Indianapolis, IN) and housed in the Mayo animal facility. For implantation of primary tumors, 1×10^7 Granta-519 cells in 100 µl of PBS were injected subcutaneously in the right rear flank of 5- to 7-week-old, female mice. Tumors were allowed to develop for ~20 days, at which point they reached ~500 mm³ and a subset of animals developed ipsilateral inguinal lymph node metastases (SCID strain only, no metastatic tumors developed in nude mice). Systemic virus administration occurred via the tail vein in a total volume of 100 µl Opti-MEM. All experiments administered 2×10^6 plaque-forming units (PFU) of virus per mouse, except for the receptor usage experiment, which used 1×10^6 PFU per mouse for all viruses. Vehicle treatment was administration of 100 µl of Opti-MEM. Animals were monitored daily for weight loss or signs of distress, and tumor volume was measured every other day using calipers and the formula $V = (a^2b) \times 0.5$, where a is the shortest and b is the longest tumor diameter. The defined tumor burden endpoint was 1,500 µl (~10% of body weight). Animals were maintained until humane euthanasia by CO_2 overdose was indicated for tumor burden or development of systemic disease symptoms including ascites, paralysis, and cachexia/weight loss. All animals receiving isotope for either imaging or radiotherapy were maintained on drinking water supplemented with 5 mg/l of L-thyroxine (Sigma-Aldrich) and iodine deficient diet (TD.95007, Harlan Laboratories) for a minimum of least 3 weeks before the first administration of isotope.

SPECT/CT imaging. Two SPECT/CT imaging systems were used: X-SPECT/CT (GammaMedica Ideas) and U-SPECTII/CT (MILabs, Utrecht, Netherlands), with the former having a reported resolution of 1–2 mm and the latter a resolution of 0.8 mm. Pertechnetate ($^{99m}TcO_4$) was administered by intraperitoneal injection at 0.5 mCi (18.5 MBq) per mouse 1 hour before imaging. Total administered dose for each animal was determined using pre- and postinjection measurements of syringe activity using a dose calibrator. Anesthesia induction was achieved using 4% isoflurane (400 µl/m) and animals were maintained under general anesthesia with 2% isoflurane (200 µl/m) for the duration of imaging by a veterinary vaporizer (Univentor 410 anesthesia unit, Zevenaar, Netherlands) and mouse-specific nose cones. Oxygen (2 l/minutes) was maintained throughout anesthesia induction and maintenance. PMOD Biomedical Image Quantification and Kinetic Modeling Software (v. 3.304; PMOD Technologies, Zürich, Switzerland) was used for volume and activity quantifications of thyroid and primary and metastatic tumor tissue.

Autoradiography and Hoechst staining. Animals with Granta-519 xenografts previously treated with MV^vac2^NIS received intraperitoneal injections of 0.5 mCi $^{99m}TcO_4$. At 50 minutes after isotope injection, mice received an IV injection of 20 mg/kg bis Benzimide H 33342 (Hoechst dye; Sigma-Aldrich). After an additional 10 minutes, mice were euthanized and tumors were harvested, weighed, and quantified for total pertechnetate activity using a dose calibrator. Tumors were then embedded in O.C.T. Compound (Tissue-Tek, Torrance, CA) and snap frozen in liquid nitrogen-cooled 2-methylbutane. 10 µmol/l tumor sections were taken at 500 µmol/l intervals throughout the entire tumor, and placed under radiographic film at −80 °C overnight. Following autoradiography, tumor sections were analyzed by confocal microscopy for Hoechst fluorescence. Color images were converted to black and white using ImageJ (version 1.46f; National Institutes of Health, Bethesda, MD) to enhance dye contrast. To analyze tumor sections following autoradiography, radiographic film was digitized to generate individual files for each section. The outermost border of tumor sections was manually delineated using ImageJ, and the diameter of this region was estimated by the average of four separate

diameter measurements. The average diameter was then used to define concentric regions of interest with 75 and 50% the radius of the outermost region. A threshold was applied based on peak background isotope levels in a time-matched vehicle control tumor, and the percent area covered by uptake was quantified for each region of interest.

Radiovirotherapy. Combination radiovirotherapy was restricted to nude mice due to pronounced radiosensitivity of SCID mice. Granta-519 xenografts were established and treated as described above. ^{131}I (1 mCi, 37 MBq) was administered by a single intraperitoneal injection 15 days after IV MV^vac2^NIS or vehicle treatment. Animals were monitored as described above.

Statistical analyses. Tumor volume and isotope uptake data were analyzed by one-way analysis of variance (single time point) or two-way repeated measures analysis of variance (multiple time points), followed by Bonferroni posttests for multiple comparisons. Survival data was analyzed using the Kaplan–Meier method and the log-rank test was used to determine the significance between groups. Prism version 5 (GraphPad Software, La Jolla, CA) was used for all statistical analysis.

SUPPLEMENTARY MATERIAL

Figure S1. MV^vac2^NIS and MV-NIS are equally cytotoxic against Granta-519 cells *in vitro*.

Figure S2. NIS expression and function *in vitro* correlates with decreased fusogenicity during MV^vac2^NIS infection.

Figure S3. SLAM but not CD46 expression sustains efficient MV^vac2^NIS replication in MCL cell lines.

Figure S4. Selective SLAM and CD46 receptor usage by MV^vac2^NIS, MV^vac2^NIS^SLAM, and MV^vac2^NIS^CD46.

Figure S5. Slower infection kinetics for Granta-519 xenografts in nude mice compared with SCID mice.

Videos S1–S4. Tomographic and three-dimensional reconstructions of the animal displayed in **Figure 5c**.

REFERENCES

1. Russell, SJ, Peng, KW and Bell, JC (2012). Oncolytic virotherapy. *Nat Biotechnol* **30**: 658–670.
2. Cattaneo, R, Miest, T, Shashkova, EV and Barry, MA (2008). Reprogrammed viruses as cancer therapeutics: targeted, armed and shielded. *Nat Rev Microbiol* **6**: 529–540.
3. Dai, G, Levy, O and Carrasco, N (1996). Cloning and characterization of the thyroid iodide transporter. *Nature* **379**: 458–460.
4. Penheiter, AR, Russell, SJ and Carlson, SK (2012). The sodium iodide symporter (NIS) as an imaging reporter for gene, viral, and cell-based therapies. *Curr Gene Ther* **12**: 33–47.
5. Dingli, D, Peng, KW, Harvey, ME, Greipp, PR, O'Connor, MK, Cattaneo, R et al. (2004). Image-guided radiovirotherapy for multiple myeloma using a recombinant measles virus expressing the thyroidal sodium iodide symporter. *Blood* **103**: 1641–1646.
6. Cortelazzo, S, Ponzoni, M, Ferreri, AJ and Dreyling, M (2012). Mantle cell lymphoma. *Crit Rev Oncol Hematol* **82**: 78–101.
7. Goy, A and Kahl, B (2011). Mantle cell lymphoma: the promise of new treatment options. *Crit Rev Oncol Hematol* **80**: 69–86.
8. M'kacher, R, Bennaceur, A, Farace, F, Laugé, A, Plassa, LF, Wittmer, E et al. (2003). Multiple molecular mechanisms contribute to radiation sensitivity in mantle cell lymphoma. *Oncogene* **22**: 7905–7912.
9. Wang, M, Oki, Y, Pro, B, Romaguera, JE, Rodriguez, MA, Samaniego, F et al. (2009). Phase II study of yttrium-90-ibritumomab tiuxetan in patients with relapsed or refractory mantle cell lymphoma. *J Clin Oncol* **27**: 5213–5218.
10. Yanagi, Y, Takeda, M and Ohno, S (2006). Measles virus: cellular receptors, tropism and pathogenesis. *J Gen Virol* **87**: 2767–2779.

11. Tatsuo, H, Ono, N, Tanaka, K and Yanagi, Y (2000). SLAM (CDw150) is a cellular receptor for measles virus. *Nature* **406**: 893–897.
12. de Swart, RL, Ludlow, M, de Witte, L, Yanagi, Y, van Amerongen, G, McQuaid, S *et al.* (2007). Predominant infection of CD150+ lymphocytes and dendritic cells during measles virus infection of macaques. *PLoS Pathog* **3**: e178.
13. Bluming, AZ and Ziegler, JL (1971). Regression of Burkitt's lymphoma in association with measles infection. *Lancet* **2**: 105–106.
14. Zygiert, Z (1971). Hodgkin's disease: remissions after measles. *Lancet* **1**: 593.
15. Dörig, RE, Marcil, A, Chopra, A and Richardson, CD (1993). The human CD46 molecule is a receptor for measles virus (Edmonston strain). *Cell* **75**: 295–305.
16. Naniche, D, Varior-Krishnan, G, Cervoni, F, Wild, TF, Rossi, B, Rabourdin-Combe, C *et al.* (1993). Human membrane cofactor protein (CD46) acts as a cellular receptor for measles virus. *J Virol* **67**: 6025–6032.
17. Galanis, E, Hartmann, LC, Cliby, WA, Long, HJ, Peethambaram, PP, Barrette, BA *et al.* (2010). Phase I trial of intraperitoneal administration of an oncolytic measles virus strain engineered to express carcinoembryonic antigen for recurrent ovarian cancer. *Cancer Res* **70**: 875–882.
18. Anderson, BD, Nakamura, T, Russell, SJ and Peng, KW (2004). High CD46 receptor density determines preferential killing of tumor cells by oncolytic measles virus. *Cancer Res* **64**: 4919–4926.
19. Ong, HT, Timm, MM, Greipp, PR, Witzig, TE, Dispenzieri, A, Russell, SJ *et al.* (2006). Oncolytic measles virus targets high CD46 expression on multiple myeloma cells. *Exp Hematol* **34**: 713–720.
20. de Vries, RD, Lemon, K, Ludlow, M, McQuaid, S, Yüksel, S, van Amerongen, G *et al.* (2010). *In vivo* tropism of attenuated and pathogenic measles virus expressing green fluorescent protein in macaques. *J Virol* **84**: 4714–4724.
21. Takeuchi, K, Nagata, N, Kato, SI, Ami, Y, Suzaki, Y, Suzuki, T *et al.* (2012). Wild-type measles virus with the hemagglutinin protein of the Edmonston vaccine strain retains wild-type tropism in macaques. *J Virol* **86**: 3027–3037.
22. Ungerechts, G, Frenzke, ME, Yaiw, KC, Miest, T, Johnston, PB and Cattaneo, R (2010). Mantle cell lymphoma salvage regimen: synergy between a reprogrammed oncolytic virus and two chemotherapeutics. *Gene Ther* **17**: 1506–1516.
23. Yaiw, KC, Miest, TS, Frenzke, M, Timm, M, Johnston, PB and Cattaneo, R (2011). CD20-targeted measles virus shows high oncolytic specificity in clinical samples from lymphoma patients independent of prior rituximab therapy. *Gene Ther* **18**: 313–317.
24. Devaux, P, von Messling, V, Songsungthong, W, Springfeld, C and Cattaneo, R (2007). Tyrosine 110 in the measles virus phosphoprotein is required to block STAT1 phosphorylation. *Virology* **360**: 72–83.
25. Parisien, JP, Bamming, D, Komuro, A, Ramachandran, A, Rodriguez, JJ, Barber, G *et al.* (2009). A shared interface mediates paramyxovirus interference with antiviral RNA helicases MDA5 and LGP2. *J Virol* **83**: 7252–7260.
26. del Valle, JR, Devaux, P, Hodge, G, Wegner, NJ, McChesney, MB and Cattaneo, R (2007). A vectored measles virus induces hepatitis B surface antigen antibodies while protecting macaques against measles virus challenge. *J Virol* **81**: 10597–10605.
27. Radecke, F, Spielhofer, P, Schneider, H, Kaelin, K, Huber, M, Dötsch, C *et al.* (1995). Rescue of measles viruses from cloned DNA. *EMBO J* **14**: 5773–5784.
28. Ohno, S, Ono, N, Takeda, M, Takeuchi, K and Yanagi, Y (2004). Dissection of measles virus V protein in relation to its ability to block alpha/beta interferon signal transduction. *J Gen Virol* **85**: 2991–2999.
29. Haralambieva, I, Iankov, I, Hasegawa, K, Harvey, M, Russell, SJ and Peng, KW (2007). Engineering oncolytic measles virus to circumvent the intracellular innate immune response. *Mol Ther* **15**: 588–597.
30. Smith, KA, Hill, SA, Begg, AC and Denekamp, J (1988). Validation of the fluorescent dye Hoechst 33342 as a vascular space marker in tumours. *Br J Cancer* **57**: 247–253.
31. Breitbach, CJ, Paterson, JM, Lemay, CG, Falls, TJ, McGuire, A, Parato, KA *et al.* (2007). Targeted inflammation during oncolytic virus therapy severely compromises tumor blood flow. *Mol Ther* **15**: 1686–1693.
32. Galanis, E (2010). Therapeutic potential of oncolytic measles virus: promises and challenges. *Clin Pharmacol Ther* **88**: 620–625.
33. Noyce, RS, Bondre, DG, Ha, MN, Lin, LT, Sisson, G, Tsao, MS *et al.* (2011). Tumor cell marker PVRL4 (nectin 4) is an epithelial cell receptor for measles virus. *PLoS Pathog* **7**: e1002240.
34. Mühlebach, MD, Mateo, M, Sinn, PL, Prüfer, S, Uhlig, KM, Leonard, VH *et al.* (2011). Adherens junction protein nectin-4 is the epithelial receptor for measles virus. *Nature* **480**: 530–533.
35. Fabre-Lafay, S, Garrido-Urbani, S, Reymond, N, Gonçalves, A, Dubreuil, P and Lopez, M (2005). Nectin-4, a new serological breast cancer marker, is a substrate for tumor necrosis factor-alpha-converting enzyme (TACE)/ADAM-17. *J Biol Chem* **280**: 19543–19550.
36. Takano, A, Ishikawa, N, Nishino, R, Masuda, K, Yasui, W, Inai, K *et al.* (2009). Identification of nectin-4 oncoprotein as a diagnostic and therapeutic target for lung cancer. *Cancer Res* **69**: 6694–6703.
37. Derycke, MS, Pambuccian, SE, Gilks, CB, Kalloger, SE, Ghidouche, A, Lopez, M *et al.* (2010). Nectin 4 overexpression in ovarian cancer tissues and serum: potential role as a serum biomarker. *Am J Clin Pathol* **134**: 835–845.
38. Biedermann, KA, Sun, JR, Giaccia, AJ, Tosto, LM and Brown, JM (1991). scid mutation in mice confers hypersensitivity to ionizing radiation and a deficiency in DNA double-strand break repair. *Proc Natl Acad Sci USA* **88**: 1394–1397.
39. Frecha, C, Costa, C, Lévy, C, Nègre, D, Russell, SJ, Maisner, A *et al.* (2009). Efficient and stable transduction of resting B lymphocytes and primary chronic lymphocyte leukemia cells using measles virus gp displaying lentiviral vectors. *Blood* **114**: 3173–3180.
40. Lenz, G and Staudt, LM (2010). Aggressive lymphomas. *N Engl J Med* **362**: 1417–1429.
41. Nourse, JP, Jones, K and Gandhi, MK (2011). Epstein-Barr Virus-related post-transplant lymphoproliferative disorders: pathogenetic insights for targeted therapy. *Am J Transplant* **11**: 888–895.
42. Howie, D, Simarro, M, Sayos, J, Guirado, M, Sancho, J and Terhorst, C (2002). Molecular dissection of the signaling and costimulatory functions of CD150 (SLAM): CD150/SAP binding and CD150-mediated costimulation. *Blood* **99**: 957–965.
43. Haddad, D, Zanzonico, PB, Carlin, S, Chen, CH, Chen, NG, Zhang, Q *et al.* (2012). A vaccinia virus encoding the human sodium iodide symporter facilitates long-term image monitoring of virotherapy and targeted radiotherapy of pancreatic cancer. *J Nucl Med* **53**: 1933–1942.
44. Jadayel, DM, Lukas, J, Nacheva, E, Bartkova, J, Stranks, G, De Schouwer, PJ *et al.* (1997). Potential role for concurrent abnormalities of the cyclin D1, p16CDKN2 and p15CDKN2B genes in certain B cell non-Hodgkin's lymphomas. Functional studies in a cell line (Granta 519). *Leukemia* **11**: 64–72.
45. Rudolph, C, Steinemann, D, Von Neuhoff, N, Gadzicki, D, Ripperger, T, Drexler, HG *et al.* (2004). Molecular cytogenetic characterization of the mantle cell lymphoma cell line GRANTA-519. *Cancer Genet Cytogenet* **153**: 144–150.
46. Kärber, G (1931). Beitrag zur kollektiven Behandlung pharmakologischer Reihenversuche. *Naunyn-Schmied Arch Pharmacol* **162**: 480–483.
47. Hubert, J (1984). Spearman-Karber method. In: *Bioassays, 2nd edn.* Hunt Publishing: Dubuque, IA. pp. 65–66.
48. Castro, MR, Bergert, ER, Beito, TG, McIver, B, Goellner, JR and Morris, JC (1999). Development of monoclonal antibodies against the human sodium iodide symporter: immunohistochemical characterization of this protein in thyroid cells. *J Clin Endocrinol Metab* **84**: 2957–2962.
49. Kakinuma, H, Bergert, ER, Spitzweg, C, Cheville, JC, Lieber, MM and Morris, JC (2003). Probasin promoter (ARR(2)PB)-driven, prostate-specific expression of the human sodium iodide symporter (h-NIS) for targeted radioiodine therapy of prostate cancer. *Cancer Res* **63**: 7840–7844.
50. Miest, TS, Yaiw, KC, Frenzke, M, Lampe, J, Hudacek, AW, Springfeld, C *et al.* (2011). Envelope-chimeric entry-targeted measles virus escapes neutralization and achieves oncolysis. *Mol Ther* **19**: 1813–1820.